Surface deformations in dynamic thermocapillary convection under partial slip

Katarzyna N. Kowal*
Department of Applied Mathematics and Theoretical Physics, University of Cambridge, Wilberforce Road, Cambridge CB3 0WA, United Kingdom, and Trinity College, University of Cambridge, Cambridge CB2 1TQ, United Kingdom

Stephen H. Davis
Department of Engineering Sciences and Applied Mathematics, Northwestern University, 2145 Sheridan Road, Evanston, Illinois 60208, USA

Peter W. Voorhees
Department of Materials Science and Engineering, Northwestern University, 2225 Campus Drive, Evanston, Illinois 60208, USA

(Received 22 April 2019; published 19 August 2019)

A prescribed, horizontal temperature gradient is imposed upon a horizontal liquid layer bounded from above by a deformable, liquid-gas interface and bounded from below by a partial-slip, rigid surface. A steady shear flow driven by thermocapillary motion emerges. This dynamic liquid layer is susceptible to the onset of oblique three-dimensional hydrothermal waves, purely two-dimensional hydrothermal waves, longitudinal traveling waves, and longitudinal rolls depending on the capillary number. A low capillary number analysis finds that surface deformations are destabilizing for all modes of instability. There is a preference for two-dimensional hydrothermal waves when there are surface deformations. Though longitudinal traveling waves are never selected as the preferred mode of instability, these waves offer a convenient way to understand the behavior of oblique hydrothermal waves, which are near-longitudinal. This is especially the case for low capillary numbers, but oblique hydrothermal waves instead tend to align themselves with the direction of flow as the capillary number increases. Surface deformations affect longitudinal waves most significantly out of all the modes of instability, especially for low Prandtl numbers. The typical length scales shorten and the critical Marangoni numbers increase with the capillary number for all types of modes. Notably, the system selects long waves near a critical Prandtl number when the interface is nondeformable and when the layer is subject to partial slip, but this is no longer the case when the upper surface is deformable.

DOI: 10.1103/PhysRevE.100.022802

I. INTRODUCTION

As a result of recent developments of additive manufacturing (AM), or three-dimensional printing (3DP) techniques, it is currently within reach to print complex structures of various geometries and materials, such as metallic, plastic, and organic parts [1–10]. Nevertheless, the current layer-by-layer production methods are impeded by numerous undesirable effects that are costly to eliminate via experimental trials alone [6,11,12]. A key limitation originates from the high-temperature gradients within the melt pool near the laser heat source, which brings about the onset of thermocapillary convection [11,13,14]. The resulting flow fields strongly affect the microstructures of the grown solid [15,16] and the rapid solidification rates common to AM and 3DP trigger complex nonlinear pattern selection [17]. These effects are potentially controllable by an appropriate adjustment of material properties, laser intensity and speed, the ambient thermal field, and various thermophysical effects.

As modeled by Ref. [16], the substrate over which material is deposited in the layer-by-layer production methods of AM can be described as providing an effective slip to the liquid film of the deposited material. This effectively stems from an average over the microstructure of the substrate and a homogenization of the mixture of solid and liquid comprising the substrate on the small scales. The liquid-to-solid fraction, and hence the effective slip, depends on the adopted production method, in which, in general, solid material deposited upon a substrate melts under a moving laser heat source and tends to resolidify in the ambient thermal field. This is a layer-by-layer process and the geometry of the finished product is shaped by the paths taken. The substrate at any given moment is either mostly solid or mostly liquid depending on whether or not the same path is continually traversed as well as on the geometry and material properties of the desired product. In general, there are inhomogeneities in the structure and composition of the substrate on scales much smaller than those of the liquid layer, which can be averaged out and built into an effective slip experienced by the liquid layer.

Previous literature on thermocapillary convection focused on static [18–20] and dynamic [16,21–24] liquid layers and flows in cavities [25–30] and in the quarter plane at high

*k.kowal@damtp.cam.ac.uk

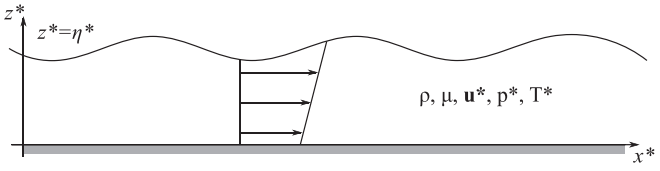

FIG. 1. Schematic of the geometry of the problem.

Marangoni number [31]. These have been supplemented by a number of experimental studies [e.g., Refs. 32–34]. When the lower boundary is a no-slip rigid surface, a dynamic liquid layer is prone to the emergence of two- and three-dimensional hydrothermal waves and longitudinal traveling waves and rolls [22]. The latter of these approach a long-wave limit at a critical Prandtl number when the lower boundary allows for slip [16]. We build upon [16], which involves thermocapillary instabilities in nondeformable liquid layers, to investigate the role of surface deformations on the selection of the preferred mode of instability, the influence on stability thresholds, trends in wave-number selection, and whether or not long waves appear.

We begin with a theoretical development in Sec. II, which lays out the governing equations, the basic state, the nondeformable limit, and an adjoint problem useful in examining contributions due to surface deformation, which are formulated at the close of this section. We follow with a discussion on longitudinal rolls in Sec. III, longitudinal traveling waves in Sec. IV, two-dimensional hydrothermal waves in Sec. V, and oblique hydrothermal waves in Sec. VI. We end with concluding remarks in Sec. VII.

II. THEORETICAL DEVELOPMENT

Motivated by the effective slip experienced by molten liquid layers in AM environments, we consider a deformable, three-dimensional liquid layer bounded by a rigid, partial-slip surface ($z^* = 0$) from below and a deformable liquid-gas interface ($z^* = \eta^*$) from above. The liquid layer is an incompressible, Newtonian fluid of mean depth d, viscosity μ, density ρ, specific heat c_p, thermal conductivity k, thermal surface conductance h, velocity $\boldsymbol{u}^*$, and pressure field p^* and is subject to an imposed horizontal temperature gradient, $\partial T^*/\partial x^* = -b$, along its upper surface, as illustrated in Fig. 1. As the film thicknesses involved are on the scale of 100 μm, gravity can be assumed to be negligible.

Thermocapillary motion results from variations in the surface tension σ_s^* of the liquid-gas interface, which decreases as a function of the temperature:

$$\sigma_s^* = \sigma_0^* - \gamma(T^* - T_0), \tag{1}$$

where T_0 is a reference value for the temperature. In dimensionless terms, this reduces to the relationship

$$\sigma_s = 1 - \mathrm{Ca}T, \tag{2}$$

involving the capillary number

$$\mathrm{Ca} = \frac{\gamma bd}{\sigma_0}, \tag{3}$$

which we assume is small but nonzero so that the interface $\eta = \eta(\boldsymbol{x}, t)$ is deformable, in contrast to the limit of zero capillary number [16], in which the interface remains flat. The nondimensionalization used is given by

$$\boldsymbol{x}^* = d\boldsymbol{x}, \quad t^* = \frac{\mu}{\gamma b}t, \quad \boldsymbol{u}^* = \frac{\gamma bd}{\mu}\boldsymbol{u}, \tag{4}$$

$$p^* = \gamma bp, \quad T^* - T_0 = bdT, \quad \sigma_s^* = \sigma_0^*\sigma_s, \tag{5}$$

where the components of the velocity vector are given by $\boldsymbol{u} = (u, v, w)$.

We assume that the upper layer is a gas of negligible density and zero pressure so that the conditions at the liquid-gas interface become

$$w = \eta_t + u\eta_x + v\eta_y, \tag{6}$$

$$\boldsymbol{\sigma}\cdot\boldsymbol{n} = -\nabla T - 2H(\mathrm{Ca}^{-1} - T)\boldsymbol{n}, \tag{7}$$

where

$$2H = -\left[\left(1+\eta_y^2\right)\eta_{xx} - 2\eta_x\eta_y\eta_{xy} + \left(1+\eta_x^2\right)\eta_{yy}\right] \times (1+|\nabla\eta|^2)^{-3/2}, \tag{8}$$

and

$$-\boldsymbol{n}\cdot\nabla T = B(T - T_\infty) + Q, \tag{9}$$

at $z = 1$, where $\boldsymbol{\sigma}$ is the stress tensor. The remaining parameters are the upper-surface Biot number

$$B = \frac{hd}{k}, \tag{10}$$

the dimensionless surface heat flux Q determined by the basic state, and the far-field temperature T_∞ of the gas. These represent the kinematic boundary condition, the thermocapillary stress conditions, and the heat flux condition at the interface.

The lower boundary exerts partial slip and no penetration, so that

$$\frac{\partial u}{\partial z} = \beta u, \quad \frac{\partial v}{\partial z} = \beta v, \quad w = 0, \quad (z = 0), \tag{11}$$

where β^{-1} is a dimensionless, effective slip parameter. We also allow for a nonzero heat flux,

$$-\boldsymbol{n}\cdot\nabla T = B_l(T - T_\infty) \quad (z = 0), \tag{12}$$

across the lower boundary in terms of the lower-boundary Biot number B_l.

The remaining equations governing the flow within the layer are given by

$$M\mathrm{Pr}^{-1}\left[\frac{\partial \boldsymbol{u}}{\partial t} + \boldsymbol{u}\cdot\nabla\boldsymbol{u}\right] = -\nabla p + \nabla^2\boldsymbol{u}, \tag{13}$$

$$\nabla\cdot\boldsymbol{u} = 0, \tag{14}$$

$$M\left[\frac{\partial T}{\partial t} + \boldsymbol{u}\cdot\nabla T\right] = \nabla^2 T, \tag{15}$$

for $0 < z < \eta$. These represent the momentum balance, incompressibility, and heat balance in dimensionless terms, in terms of the Prandtl number Pr and Marangoni number M,

where

$$\mathrm{Pr} = \frac{M}{R} = \frac{\mu c_p}{k}, \quad M = \frac{\rho\gamma b d^2 c_p}{\mu k}. \tag{16}$$

Here,

$$R = \frac{\rho\gamma b d^2}{\mu^2} \tag{17}$$

is the Reynolds number. The remaining dimensionless parameters are the previously defined effective slip parameter β^{-1}, the upper- and lower-layer Biot numbers B and B_l, respectively, and the capillary number Ca.

A. Basic state

We consider the partial-slip shear-flow solution given by

$$\bar{u} = z + \beta^{-1}, \quad \bar{v} = \bar{w} = 0, \quad \bar{p} = 0, \tag{18}$$

$$\begin{aligned}\bar{T} = &-x + M\left[\frac{1}{6}(1-z^3) + \frac{1}{2\beta}(1-z^2)\right.\\ &\left. + B^{-1}\left(\frac{1}{2}+\frac{1}{\beta}\right) + QM^{-1}B^{-1}\right]\\ &- B_l\gamma[1 + B(1-z)],\end{aligned} \tag{19}$$

where

$$\gamma = \frac{M[3(\beta+2) + (\beta+3)B] - 6\beta Q}{6\beta B(BB_l + B + B_l)} \tag{20}$$

is a constant. The temperature of the bounding gas is externally imposed to have a linear, horizontal gradient,

$$T_\infty = -x. \tag{21}$$

The continuity of temperature at the upper interface fixes Q,

$$Q = \frac{M[3\beta + (2\beta+3)B_l + 6]}{6\beta(B_l+1)}, \tag{22}$$

so that

$$\bar{T} = -x - \frac{M(z-1)[z(z\beta+\beta+3)(B_l+1) + 3 + \beta]}{6\beta(B_l+1)}. \tag{23}$$

The limits $\beta \to \infty$ and $B_l = 0$ recover the basic state of Ref. [22].

B. Nondeformable limit: Ca = 0

We expand in the small parameter Ca and introduce perturbations $X = \bar{X} + \epsilon X' + \cdots$, where $X = (\boldsymbol{u}, p, T, \eta)$ and $X' = (\boldsymbol{u}_0, p_0, T_0, \eta_0) + \mathrm{Ca}(\boldsymbol{u}_1, p_1, T_1, \eta_1) + \cdots$. The problem at zeroth-order in Ca, for which the interface remains flat, $\eta_0 = 1$, has been formulated by Ref. [16]. We state the corresponding equations in this limit as follows, for completeness:

$$M_0\mathrm{Pr}^{-1}\left[\frac{\partial \boldsymbol{u}_0}{\partial t} + \bar{u}\frac{\partial \boldsymbol{u}_0}{\partial x} + w_0\frac{\partial \bar{u}}{\partial z}\boldsymbol{e_x}\right] = -\boldsymbol{\nabla} p_0 + \nabla^2 \boldsymbol{u}_0, \tag{24}$$

$$M_0\left[\frac{\partial T_0}{\partial t} + \bar{u}\frac{\partial T_0}{\partial x} + u_0\frac{\partial \bar{T}}{\partial x} + w_0\frac{\partial \bar{T}}{\partial z}\right] = \nabla^2 T_0, \tag{25}$$

$$\boldsymbol{\nabla}\cdot\boldsymbol{u}_0 = 0, \tag{26}$$

with the boundary conditions

$$w_0 = 0 \quad (z=1), \tag{27}$$

$$\frac{\partial u_0}{\partial z} + \frac{\partial w_0}{\partial x} = -\frac{\partial T_0}{\partial x} \quad (z=1), \tag{28}$$

$$\frac{\partial v_0}{\partial z} + \frac{\partial w_0}{\partial y} = -\frac{\partial T_0}{\partial y} \quad (z=1), \tag{29}$$

$$-\frac{\partial T_0}{\partial z} = BT_0 \quad (z=1), \tag{30}$$

$$\frac{\partial u_0}{\partial z} = \beta u_0, \quad \frac{\partial v_0}{\partial z} = \beta v_0, \quad w_0 = 0 \quad (z=0), \tag{31}$$

$$\frac{\partial T_0}{\partial z} = B_l T_0 \quad (z=0). \tag{32}$$

We are interested in normal mode solutions:

$$(\boldsymbol{u}_0, p_0, T_0) = [\hat{u}_0(z), \hat{p}_0(z), \hat{T}_0(z)]e^{\sigma_0 t + i\boldsymbol{\alpha}\cdot\boldsymbol{x}}, \tag{33}$$

where $\boldsymbol{\alpha} = (\alpha_1, \alpha_2, 0)$, $\alpha = |\boldsymbol{\alpha}|$, and we eliminate $\hat{p}$ and $\hat{v}$ to obtain a reduced system of differential equations for the problem at zeroth order in Ca.

This gives an eighth-order eigenvalue problem, which we solve numerically. We are, in particular, interested in neutral stability and write $\sigma = i\omega$, where ω is the angular frequency, to obtain the neutral curve in terms of the Marangoni number,

$$M_0 = M_0(\alpha_1, \alpha_2, \mathrm{Pr}, B, B_l, \beta), \tag{34}$$

and frequency,

$$\omega_0 = \omega_0(\alpha_1, \alpha_2, \mathrm{Pr}, B, B_l, \beta). \tag{35}$$

C. Adjoint problem

In order to solve the problem at first order in the capillary number, it is useful to formulate the adjoint problem at zeroth order. We denote the adjoint solution by $\tilde{X}_0 = (\tilde{\boldsymbol{u}}_0, \tilde{p}_0, \tilde{T}_0, \tilde{\eta}_0)$. Note the difference in notation between the original solution $\hat{X}_0$ and the adjoint solution $\tilde{X}_0$. By taking inner products and integrating, we find the following adjoint equations:

$$\begin{aligned}&M_0\mathrm{Pr}^{-1}[i\alpha_1(z+\beta^{-1}) + \sigma_0]u_0 + \alpha^2\tilde{u}_0 - \tilde{u}_0''\\ &\quad - M_0\tilde{T}_0 + i\alpha_1\tilde{p}_0 = 0,\end{aligned} \tag{36}$$

$$\begin{aligned}&M_0\mathrm{Pr}^{-1}[i\alpha_1(z+\beta^{-1}) + \sigma_0]\tilde{v}_0 + \alpha^2\tilde{v}_0 - \tilde{v}_0''\\ &\quad + i\alpha_2\tilde{p}_0 = 0,\end{aligned} \tag{37}$$

$$\begin{aligned}&M_0\mathrm{Pr}^{-1}\tilde{u}_0 + M_0\mathrm{Pr}^{-1}[i\alpha_1(z+\beta^{-1}) + \sigma_0]\tilde{w}_0\\ &\quad + \alpha^2\tilde{w}_0 - \tilde{w}_0'' - M_0^2(2^{-1}z^2 + \beta^{-1}z)\tilde{T}_0 - \tilde{p}_0' = 0,\end{aligned} \tag{38}$$

$$M_0[i\alpha_1(z+\beta^{-1}) + \sigma_0]\tilde{T}_0 + \alpha^2\tilde{T}_0 - \tilde{T}_0'' = 0, \tag{39}$$

$$i\alpha_1\tilde{u}_0 + i\alpha_2\tilde{v}_0 - \tilde{w}_0' = 0, \tag{40}$$

subject to the boundary conditions

$$\tilde{u}_0' = \beta\tilde{u}_0, \quad \tilde{v}_0' = \beta\tilde{v}_0, \quad w_0 = 0, \quad T_0' = B_l T_0, \tag{41}$$

at $z = 0$, and

$$\tilde{u}_0' = 0, \quad \tilde{v}_0' = 0, \quad \tilde{w}_0 = 0, \tag{42}$$

$$i\alpha_1\tilde{u}_0 + i\alpha_2\tilde{v}_0 + B\tilde{T}_0 + \tilde{T}_0' = 0, \tag{43}$$

at $z = 1$.

This, too, gives an eighth-order eigenvalue problem, which can be solved numerically. We can similarly obtain the neutral curve in terms of the Marangoni number, which coincides with the neutral curve for the original problem. Quantities of interest to us for the next-order problem are the adjoint solutions $\tilde{X}_0$.

D. Surface deformations

We formulate the problem at the next order in the capillary number in terms of the operators $\boldsymbol{\mathcal{L}_1}, \ldots, \boldsymbol{\mathcal{L}_5}$, the functions $\boldsymbol{\phi^{(0)}} = (u_0, v_0, w_0, T_0, p_0)$ and $\boldsymbol{\phi^{(1)}} = (u_1, v_1, w_1, T_1, p_1)$, and a matrix $\boldsymbol{F}$, which is specified below. The governing equations can be summarized by

$$\boldsymbol{\mathcal{L}} \cdot \boldsymbol{\phi^{(1)}} = \boldsymbol{F} \cdot \boldsymbol{\phi^{(0)}}, \tag{44}$$

where $\boldsymbol{\mathcal{L}} = (\boldsymbol{\mathcal{L}_1}, \ldots, \boldsymbol{\mathcal{L}_5})$;

$$\begin{aligned}\boldsymbol{\mathcal{L}_1} \cdot \boldsymbol{\phi^{(1)}} =& M_0\mathrm{Pr}^{-1}[i\alpha_1 z u_1 + (i\alpha_1\beta^{-1} + \sigma_0)u_1 + w_1] \\ &+ i\alpha_1 p_1 + \alpha^2 u_1 - u_1'',\end{aligned} \tag{45}$$

$$\begin{aligned}\boldsymbol{\mathcal{L}_2} \cdot \boldsymbol{\phi^{(1)}} =& M_0\mathrm{Pr}^{-1}[i\alpha_1 z v_1 + (i\alpha_1\beta^{-1} + \sigma_0)v_1] \\ &+ i\alpha_2 p_1 + \alpha^2 v_1 - v_1'',\end{aligned} \tag{46}$$

$$\begin{aligned}\boldsymbol{\mathcal{L}_3} \cdot \boldsymbol{\phi^{(1)}} =& M_0\mathrm{Pr}^{-1}[i\alpha_1 z w_1 + (i\alpha_1\beta^{-1} + \sigma_0)w_1] \\ &+ p_1' + \alpha^2 w_1 - w_1'',\end{aligned} \tag{47}$$

$$\begin{aligned}\boldsymbol{\mathcal{L}_4} \cdot \boldsymbol{\phi^{(1)}} =& M_0[i\alpha_1 z T_1 + (i\alpha_1\beta^{-1} + \sigma_0)T_1 - u_1 \\ &- M_0(2^{-1}z^2 + \beta^{-1}z)w_1] + \alpha^2 T_1 - T_1'',\end{aligned} \tag{48}$$

$$\boldsymbol{\mathcal{L}_5} \cdot \boldsymbol{\phi^{(1)}} = i\alpha_1 u_1 + i\alpha_2 v_1 + w_1'; \tag{49}$$

and

$$\begin{aligned}[\boldsymbol{F} \cdot \boldsymbol{\phi^{(0)}}]_1 =& -\mathrm{Pr}^{-1}\{M_1[i\alpha_1(z + \beta^{-1}) + \sigma_0] \\ &+ M_0\sigma_1\}u_0 - M_1\mathrm{Pr}^{-1}w_0,\end{aligned} \tag{50}$$

$$[\boldsymbol{F} \cdot \boldsymbol{\phi^{(0)}}]_2 = -\mathrm{Pr}^{-1}\{M_1[i\alpha_1(z + \beta^{-1}) + \sigma_0] + M_0\sigma_1\}v_0, \tag{51}$$

$$[\boldsymbol{F} \cdot \boldsymbol{\phi^{(0)}}]_3 = -\mathrm{Pr}^{-1}\{M_1[i\alpha_1(z + \beta^{-1}) + \sigma_0] + M_0\sigma_1\}w_0, \tag{52}$$

$$\begin{aligned}[\boldsymbol{F} \cdot \boldsymbol{\phi^{(0)}}]_4 =& -\{M_1[i\alpha_1(z + \beta^{-1}) + \sigma_0] + M_0\sigma_1\}T_0 \\ &+ M_1 u_0 + M_0 M_1(z^2 + 2\beta^{-1}z)w_0,\end{aligned} \tag{53}$$

$$[\boldsymbol{F} \cdot \boldsymbol{\phi^{(0)}}]_5 = 0. \tag{54}$$

These are supplemented by the boundary conditions

$$w_1 = [i\alpha_1(1 + \beta^{-1}) + \sigma_0]\eta_1, \tag{55}$$

$$i\alpha_1 w_1 + u_1' = -i\alpha_1 T_1, \tag{56}$$

$$i\alpha_2 w_1 + v_1' = -i\alpha_2 T_1, \tag{57}$$

$$\begin{aligned}&[M_0(1 + \beta^{-1}) - i\alpha_1]\eta_1 - T_1' \\ &\quad = -BM_0(2^{-1} + \beta^{-1})\eta_1 + BT_1,\end{aligned} \tag{58}$$

$$p_0 + 2w_0' = -\alpha^2\eta_1 - T_0', \tag{59}$$

at $z = 1$, and

$$u_1' = \beta u_1, \quad v_1' = \beta v_1, \quad w_1 = 0, \tag{60}$$

$$T_1' = B_l T_1, \tag{61}$$

at $z = 0$.

We obtain a solvability condition by forming the inner product

$$(\tilde{\boldsymbol{\phi}}^{\boldsymbol{(0)}}, \boldsymbol{\mathcal{L}} \cdot \boldsymbol{\phi^{(1)}}) = (\tilde{\boldsymbol{\phi}}^{\boldsymbol{(0)}}, \boldsymbol{F} \cdot \boldsymbol{\phi^{(0)}}), \tag{62}$$

where $(f, g) = \int_0^1 f(z)g(z)dz$. Noting that $\tilde{\boldsymbol{\phi}}^{\boldsymbol{(0)}}$ solves the adjoint problem and reducing, we obtain the solvability condition explicitly as follows:

$$\begin{aligned}&\eta_1[(i\alpha_1\tilde{u}_0 + i\alpha_2\tilde{v}_0 + \tilde{w}_0')[i\alpha_1(1 + \beta^{-1}) + \sigma_0] \\ &\quad - \tilde{T}_0[M_0(1 + \beta^{-1}) - i\alpha_1 + BM_0(2^{-1} + \beta^{-1})]]_{z=1} \\ &\quad = \sigma_1 I_1 + M_1 I_2,\end{aligned} \tag{63}$$

where the integrals I_1 and I_2 are defined by

$$I_1 = -\int_0^1 M_0[\mathrm{Pr}^{-1}(\tilde{u}_0 u_0 + \tilde{v}_0 v_0 + \tilde{w}_0 w_0) + \tilde{T}_0 T_0]dz, \tag{64}$$

$$\begin{aligned}I_2 =& -\int_0^1 \{[i\alpha_1(z + \beta^{-1}) + \sigma_0][\mathrm{Pr}^{-1}(\tilde{u}_0 u_0 + \tilde{v}_0 v_0 \\ &+ \tilde{w}_0 w_0) + \tilde{T}_0 T_0] + \mathrm{Pr}^{-1}\tilde{u}_0 w_0 \\ &+ \tilde{T}_0[u_0 + M_0(z^2 2\beta^{-1}z)w_0]\}dz.\end{aligned} \tag{65}$$

The solvability condition (63) determines σ_1 and M_1 in terms of quantities known at zeroth order in Ca. Note that the surface deformation η_1 can be determined from Eq. (59) in terms of known quantities.

III. LONGITUDINAL ROLLS

Longitudinal instabilities occur when $\alpha_1 = 0$. Longitudinal rolls are a type of longitudinal instability for which $\omega = 0$. Physically, these are seen as rolls aligned along the x axis.

Typical neutral curves for longitudinal rolls are shown in Fig. 2 for both $\mathrm{Ca} = 0$ and $\mathrm{Ca} \neq 0$. The region of instability expands when the capillary number is allowed to be nonzero. The critical Marangoni number, necessary for the onset of instability, increases moderately with the capillary number as shown in Fig. 3(a). The critical wave number corresponding to this is also seen to increase with the capillary number as

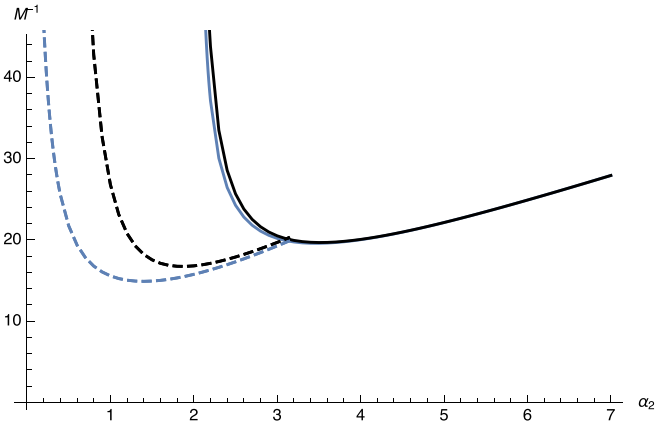

FIG. 2. Neutral curves depicting the inverse Marangoni number for longitudinal traveling waves (dashed lines) and longitudinal rolls (solid lines) for $\mathrm{Ca} = 0$ [blue (gray) lines] and $\mathrm{Ca} = 0.1$ (black lines).

shown in Fig. 3(b). That is, when the interface is deformable, the system is more prone to the onset of longitudinal rolls and their typical length scales are shorter.

The critical Marangoni number for the onset of longitudinal rolls is depicted as a function of the Prandtl number in Fig. 4(a) for both $\mathrm{Ca} = 0$ and $\mathrm{Ca} \neq 0$. The effect of surface deformations is weak for low Prandtl numbers; the

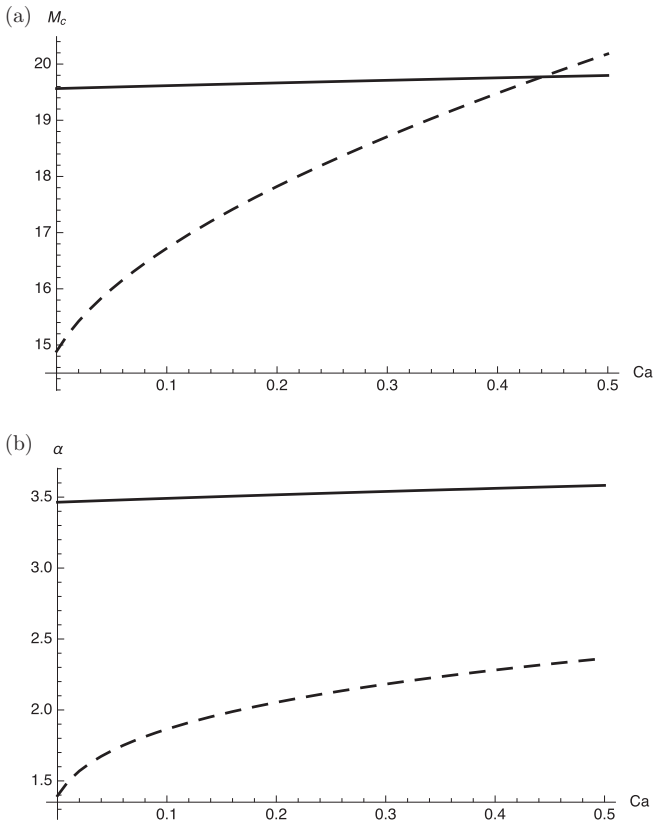

FIG. 3. (a) The critical Marangoni number and (b) the critical wave number for longitudinal rolls (solid lines) and longitudinal traveling waves (dashed lines) versus the capillary number.

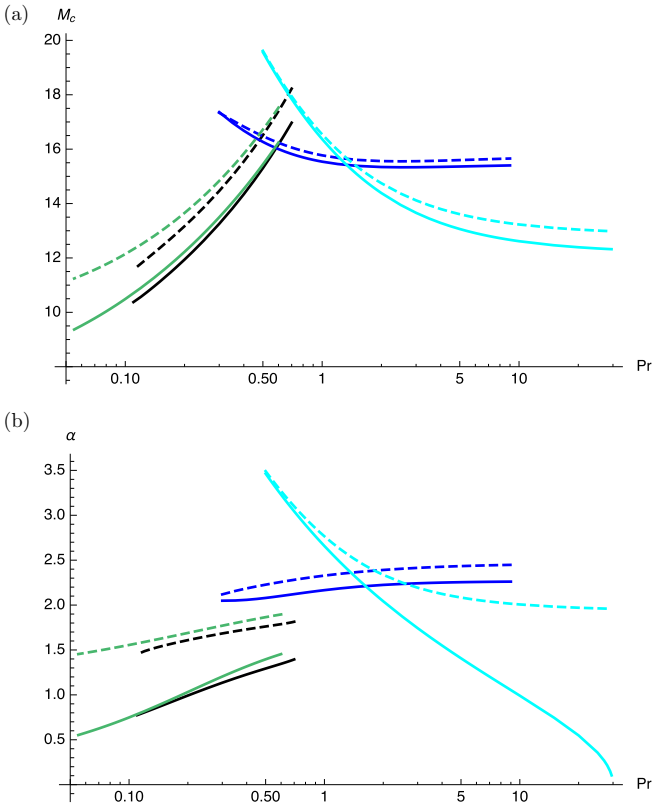

FIG. 4. Neutral curves depicting (a) the critical Marangoni number and (b) the magnitude of the wave vector for each Prandtl number for oblique waves (black lines), longitudinal traveling waves (green lines), two-dimensional modes (blue lines), and longitudinal rolls (cyan lines) for $\mathrm{Ca} = 0$ (solid lines) and $\mathrm{Ca} = 0.1$ (dashed lines). The minimal Marangoni number for each mode at a given value of Pr defines the preferred mode of instability.

critical Marangoni numbers for $\mathrm{Ca} = 0$ and $\mathrm{Ca} \neq 0$ are close to each other in this range. Surface deformations begin to play a more significant role for large Prandtl numbers. The critical Marangoni number for $\mathrm{Ca} \neq 0$ is significantly larger than that for $\mathrm{Ca} = 0$ for this range of Prandtl numbers. A major difference is that the system selects long waves for $\mathrm{Ca} = 0$ near a critical Prandtl number $\mathrm{Pr} = \mathrm{Pr}_c$, defined as the maximal Prandtl number for which instabilities occur [$\mathrm{Pr}_c \approx 30$ in Fig. 4(b)], but this is no longer the case when $\mathrm{Ca} \neq 0$. This can be seen in Fig. 4(b) near $\mathrm{Pr} = \mathrm{Pr}_c$. The critical

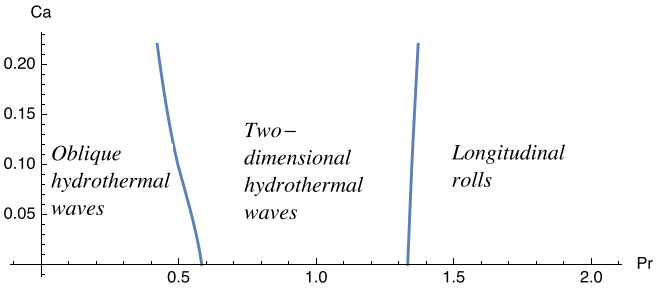

FIG. 5. Regime diagram depicting the preferred modes of instability in (Ca, Pr) space.

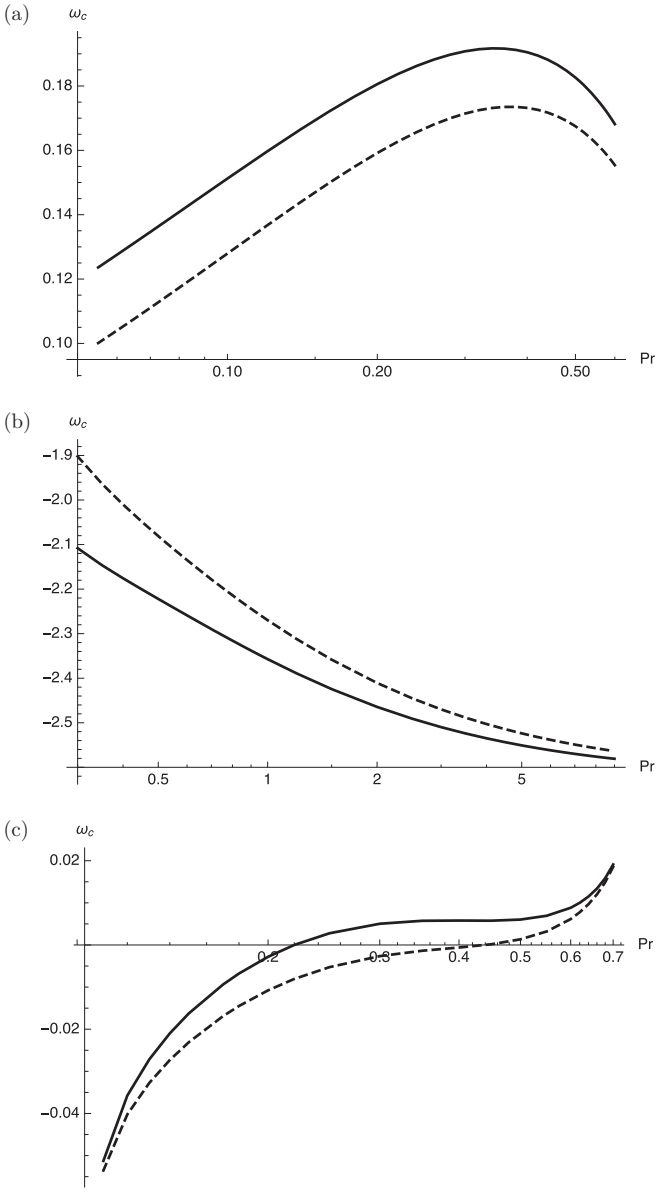

FIG. 6. The critical frequency for (a) longitudinal traveling waves, (b) two-dimensional hydrothermal waves, and (c) oblique hydrothermal waves versus the Prandtl number for Ca = 0 (solid lines) and Ca = 0.1 (dashed lines).

wave number decreases towards 0 as $\mathrm{Pr} \to \mathrm{Pr}_c$ for Ca = 0; however, it remains bounded away from 0 when Ca ≠ 0.

Longitudinal rolls are the preferred mode of instability for large Prandtl numbers. This range of Prandtl numbers reduces with the capillary number, but does so only weakly as seen in Fig. 5, in favor of two-dimensional hydrothermal waves, which become selected instead.

IV. LONGITUDINAL TRAVELING WAVES

Longitudinal traveling waves are a type of longitudinal instability for which the frequency $\omega \neq 0$. Physically, these are seen as waves aligned along the x axis and traveling in the direction orthogonal to it.

Typical neutral curves for longitudinal waves are shown in Fig. 2 for Ca = 0 and Ca ≠ 0. Neutral curves for Ca ≠ 0 depart significantly from those for which Ca = 0, in comparison to the neutral curves for longitudinal rolls. The region of instability expands significantly when the capillary number is taken to be nonzero. This occurs for all Prandtl numbers for which longitudinal hydrothermal waves are the near-dominant mode of instability, as seen in Fig. 4(a). The departure of the critical Marangoni number as the capillary number is taken to be nonzero is among the largest for longitudinal traveling waves in comparison to the remaining modes of instability. This departure for longitudinal traveling waves is largest for low Prandtl numbers.

Similarly to the case in which there are no surface deformations, the neutral curves, and therefore the critical Marangoni number, for longitudinal traveling waves are close to another mode of instability, namely, close to oblique hydrothermal waves which are discussed in Sec. VI. These two modes are closest to each other for large Prandtl numbers and the oblique mode is always more unstable. This amounts to Pr ∼ 0.4–0.6 in the range for which the oblique mode is selected by the system as the dominant mode of instability among all modes. Despite never being selected by the system, longitudinal traveling waves offer a simple way to understand the behavior of oblique hydrothermal waves, which are near-longitudinal in instances in which these modes are the dominant mode of instability.

The critical Marangoni number for longitudinal traveling waves increases monotonically with the capillary number as shown in Fig. 3(a), in comparison to the critical Marangoni number for longitudinal rolls. The two modes exchange stability for high enough capillary number (Ca ∼ 0.42). The critical wave number increases with Ca similarly, as shown in Fig. 3(b). Even though the critical wave number for longitudinal waves increases at a rate faster than that for longitudinal modes, these two wave numbers do not coincide at any capillary number.

The corresponding critical wave numbers are shown in Fig. 4(b). The critical wave numbers of the two modes (longitudinal and oblique hydrothermal waves) are closest to each other when there are no surface deformations. This is particularly the case for low Prandtl numbers.

The critical frequency decreases when there are surface surface deformations, as shown in Fig. 6(a). This occurs for all relevant Prandtl numbers. The general behavior, however, remains the same as for the case in which there are no surface deformations.

V. TWO-DIMENSIONAL HYDROTHERMAL WAVES

Two-dimensional hydrothermal waves are modes which do not involve the cross-flow direction, that is, modes for which $\alpha_2 = 0$. These are seen as waves propagating along the mean flow direction without any cross-flow component.

Two-dimensional hydrothermal waves are selected by the system as the dominant mode of instability for intermediate Prandtl numbers, as seen in Fig. 5. These waves are more common when surface deformations are allowed. As the capillary number increases, the range of Prandtl numbers for which these waves are the dominant mode of instability expands, as

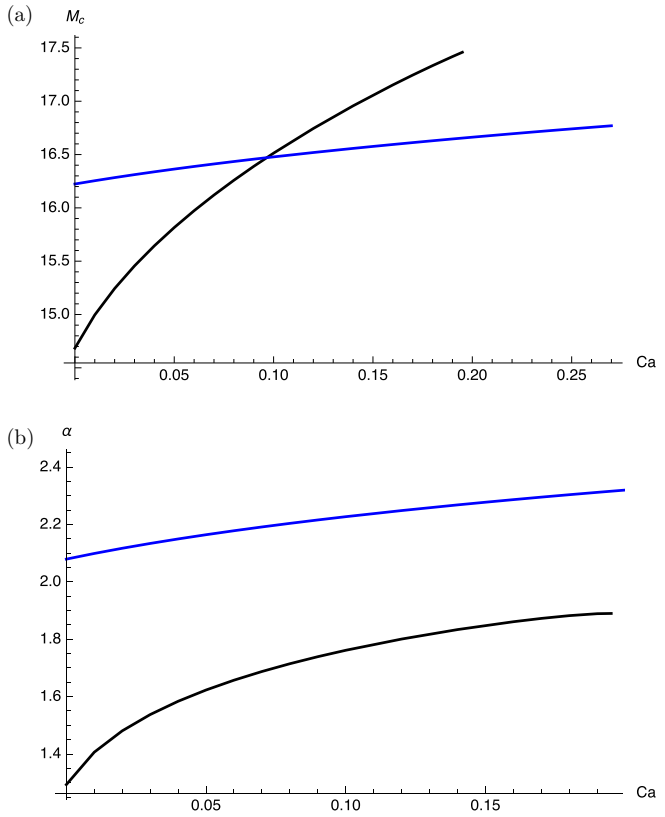

FIG. 7. (a) The critical Marangoni number and (b) the magnitude of the critical wave vector for oblique hydrothermal waves (black lines) and two-dimensional hydrothermal waves [blue (gray) lines] versus the capillary number.

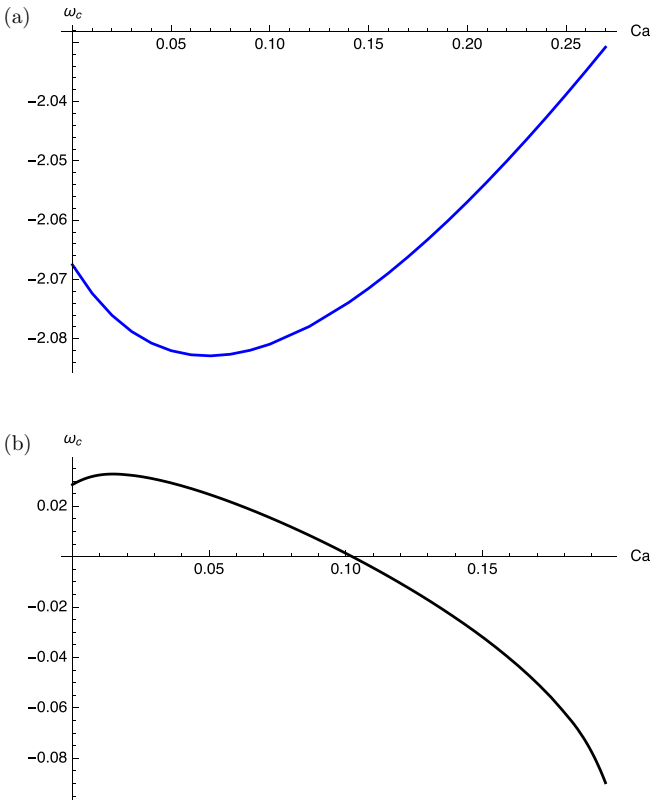

FIG. 8. The critical frequency versus the capillary number for (a) two-dimensional hydrothermal waves and (b) oblique hydrothermal waves.

seen in Fig. 5. These two-dimensional hydrothermal waves appear for more Prandtl numbers instead of longitudinal rolls and, particularly, oblique hydrothermal waves.

Neutral curves depicting the critical Marangoni number for two-dimensional hydrothermal waves are shown in Fig. 4(a), in comparison to the other modes of instability, for $\mathrm{Ca} = 0$ and $\mathrm{Ca} \neq 0$. Surface deformations affect these modes most for large Prandlt numbers. The corresponding critical wave number for two-dimensional modes is shown in Fig. 4(b), in which the effect of surface deformation is similarly seen most visibly for large Prandtl numbers. The critical Marangoni number and the critical wave number both increase with the capillary number, as seen in Fig. 7.

The magnitude of the frequency of these waves is, in general, smaller with surface deformations than without, as seen in Fig. 6. However, this is only the case for large enough capillary numbers, as the magnitude of the critical frequency is seen to initially increase with the capillary number, until it decreases for $\mathrm{Ca} \gtrapprox 0.07$, as seen in Fig. 8.

VI. OBLIQUE HYDROTHERMAL WAVES

Oblique hydrothermal waves are the most general type of mode. For these waves, $\alpha_1 \neq 0$, $\alpha_2 \neq 0$, and $\omega \neq 0$. Physically, these are seen as waves traveling at an angle ϕ to the x axis, where $\phi \neq 0$.

Oblique hydrothermal waves are selected by the system as the dominant mode of instability for low Prandtl numbers, as seen in Fig. 5. However, the range of Prandtl numbers for which these modes dominate reduces with the capillary number. When there are surface deformations, oblique waves are less common. This occurs in favor of two-dimensional hydrothermal waves, which appear instead.

The critical Marangoni number for oblique hydrothermal waves is shown in Fig. 4(a), in comparison to other modes along with the magnitude of the critical wave vector in Fig. 4(b) for $\mathrm{Ca} = 0$ and $\mathrm{Ca} \neq 0$. In particular, these modes are seen to be near-longitudinal and their critical Marangoni numbers are seen to be close to those of purely longitudinal hydrothermal waves. However, oblique hydrothermal waves appear to become less near-longitudinal as the capillary number increases. This is seen in Fig. 9(a), where the critical wave vector for oblique hydrothermal waves is seen to be further away from the α_2 axis than for the nondeformable limit for all Prandtl numbers. In fact, both components of the critical wave vector grow with the capillary number as shown in Fig. 9(b). The character of the variation of the wave vector with the Prandtl number changes once surface deformations are allowed. Namely, with surface deformations, these waves no longer become more near-longitudinal as the Prandtl number decreases.

Surface deformations decrease the critical frequency of oblique hydrothermal waves for all Prandtl numbers for which these waves dominant, as shown in Fig. 6. The decrease is most apparent for intermediate Prandtl numbers.

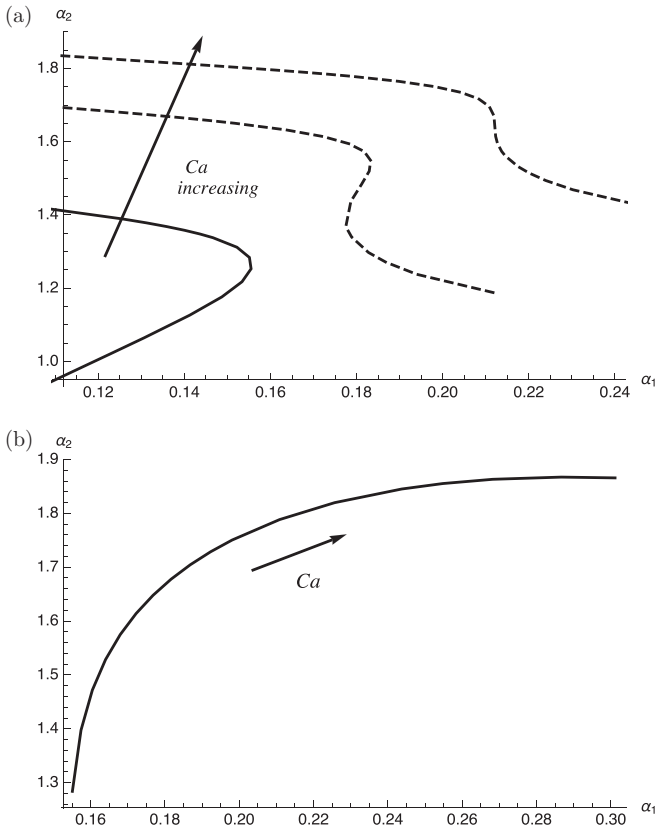

FIG. 9. The critical wave vector (α_1, α_2) for oblique hydrothermal waves (a) as Pr varies for $\mathrm{Ca} = 0$ (solid lines) and $\mathrm{Ca} = 0.05, 0.1$ (dashed lines)—these are the nondeformable and deformable branches—and (b) at a fixed value of $\mathrm{Pr} = 1/2$ as the capillary number varies.

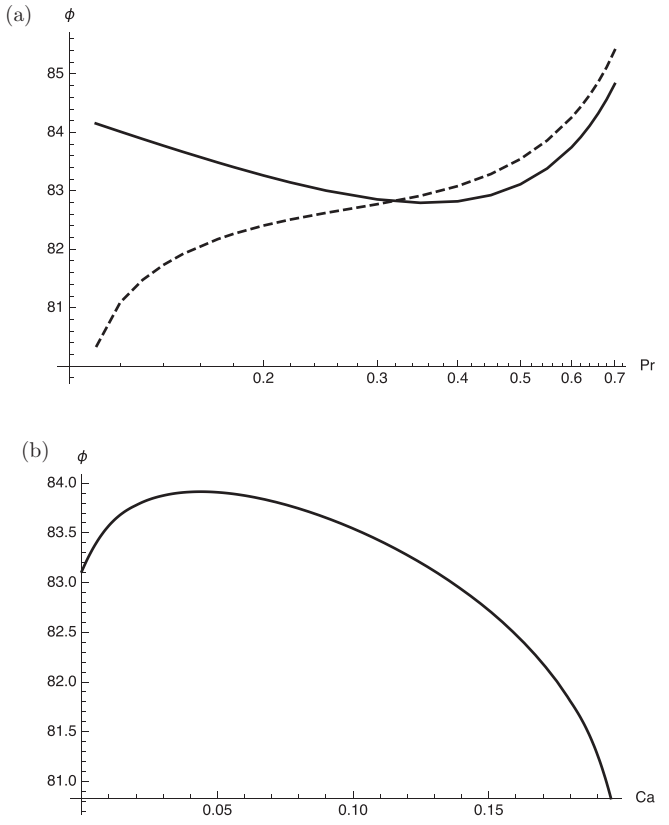

FIG. 10. The angle of inclination of the critical wave vector for oblique hydrothermal waves (a) versus the Prandtl number for $\mathrm{Ca} = 0$ (solid lines) and $\mathrm{Ca} = 0.1$ (dashed lines) and (b) versus the capillary number.

The corresponding magnitude of the critical wave vector is shown in Fig. 7(b), which is seen to increase steadily with the capillary number. The critical frequency for oblique hydrothermal waves initially increases until $\mathrm{Ca} \sim 0.1$, followed by a rapid decrease in frequency for larger capillary numbers.

The critical Marangoni number for oblique hydrothermal waves increases monotonically with the capillary number as shown in Fig. 7(a), triggering an exchange of stability with two-dimensional hydrothermal waves. Even though oblique waves are preferred by the system for $\mathrm{Ca} = 0$ and for low enough capillary numbers, there is an exchange of stability for $\mathrm{Ca} \sim 0.1$ and two-dimensional waves become preferred for larger values of Ca. The angle of inclination ϕ for oblique waves is shown in Fig. 10 for $\mathrm{Ca} = 0$ and $\mathrm{Ca} \neq 0$, where a decrease from 90° is seen as the Prandtl number decreases. The angle of inclination is also shown for a fixed Prandtl number as a function of the capillary number in Fig. 10(b), where it is seen to initially increase, followed by a sharp decrease from 90° with the capillary number.

VII. CONCLUSIONS

We have investigated the onset of hydrothermal instabilities in a dynamic, horizontal liquid layer, with a deformable, upper liquid-gas surface and a rigid lower boundary that allows for slip. The system is susceptible to the onset of oblique three-dimensional hydrothermal waves, purely two-dimensional hydrothermal waves, longitudinal traveling waves, and longitudinal rolls. These result from an imposed horizontal temperature gradient along the upper interface, which in turn makes the liquid layer dynamic as opposed to static. We perform a low capillary number analysis and find that the capillary number intricately affects the preferred mode of instability.

We find that surface deformations are destabilizing and the region of parameter space for which the system is unstable expands for all modes of instability. However, there is a preference towards two-dimensional hydrothermal waves as the capillary number increases. These are preferable for intermediate Prandtl numbers, followed by longitudinal rolls for large Prandtl numbers. The range of Prandtl numbers for which longitudinal modes are selected by the system reduces with the capillary number in favor of two-dimensional waves, but does so only weakly. The system is more prone to the onset of longitudinal rolls when the interface is deformable and their typical length scales are shorter. The effect of surface deformations is weak for longitudinal rolls at low Prandtl numbers, but becomes significant for large Prandtl numbers. A key difference is that the system selects long waves near a critical Prandtl number $\mathrm{Pr} = \mathrm{Pr}_c$ when the interface is nondeformable and when the layer is subject to partial slip, but this is no longer the case when surface deformations are allowed

as the critical wave number remains bounded away from zero for $\mathrm{Ca} \neq 0$.

Hydrothermal waves traveling longitudinally along the direction of flow are never selected by the system. However, these waves offer a simple way to understand the behavior of oblique hydrothermal waves as these are near-longitudinal whenever they are selected. Surface deformations affect longitudinal waves most significantly out of all the modes of instability, for all Prandtl numbers for which these waves are the near-dominant mode of instability. However, this effect is largest for low Prandtl numbers. Both with and without surface deformations, longitudinal and oblique hydrothermal waves are closest to each other for large Prandtl numbers, but oblique waves are always more unstable. The critical wave numbers of these two modes are closest to each other when there are no surface deformations, especially for low Prandtl numbers. Longitudinal waves and rolls exchange stability for high enough capillary number and the critical Marangoni number and critical wave number increase monotonically with the capillary number for both of these modes. The critical wave number for longitudinal waves is always smaller than that of longitudinal rolls, even though it increases at a faster rate for longitudinal waves. The critical frequency for longitudinal waves decreases with the capillary number for all relevant Prandtl numbers. The general behavior, however, remains unchanged.

Two-dimensional hydrothermal waves are the preferred mode of instability for intermediate Prandtl numbers, and these waves become more dominant as the capillary number increases. Surface deformations affect these modes most for large Prandtl numbers. The critical wave number for these waves is similarly affected most visibly for large Prandtl numbers. Both the critical Marangoni number and the critical wave number both increase with the capillary number. The magnitude of the frequency of these waves decreases with the capillary number but only for large enough capillary numbers, preceded by an initial increase for small Ca.

The system selects oblique hydrothermal waves for low Prandtl numbers. However, these waves are less common when there are surface deformations and two-dimensional hydrothermal waves are selected instead. Oblique hydrothermal waves are shown to be near-longitudinal and the critical Marangoni number closely follows that of purely longitudinal hydrothermal waves for low capillary numbers. As the capillary number increases, these waves become less near-longitudinal, instead tending to align themselves with the direction of flow. The magnitude of the wave vector grows with the capillary number. Notably, as the Prandtl number decreases, these waves become more near-longitudinal in the nondeformable limit. This is no longer the case when there are surface deformations. A sharp decrease of the angle of inclination from 90° is seen as the Prandtl number decreases. When the Prandtl number is fixed, the angle of inclination initially increases, followed by a sharp decrease from 90° when the capillary number increases. The critical frequency of these waves rapidly decreases for all relevant Prandtl numbers, most notably for intermediate Prandtl numbers, when the interface is deformable and the capillary number is large enough. However, there is an initial increase in the frequency for low capillary numbers, up to $\mathrm{Ca} \sim 0.1$. The critical Marangoni number for oblique waves increases with the capillary number at a rate lower than that for two-dimensional hydrothermal waves, triggering an exchange of stability between these two modes at $\mathrm{Ca} \sim 0.1$.

Our results imply that melt pools in the context of AM are more susceptible to the onset of thermocapillary convection when surface tension is moderate enough to allow for surface deformation, in contrast to scenarios in which there are no surface deformations. The resulting flow fields affect the microstructures of the finished product after solidification. In particular, microstructures of alternate layers, or bands, of dendrites, cells, and homogenous material seen in experiments on metallic systems [35–38] appear for lower solidification rates with such a flow than without it and may disappear completely when the magnitude of the flow is large enough [15,39].

ACKNOWLEDGMENTS

This work is supported by the National Institute of Standards and Technology (Grant No. 70NANB14H012) as part of the Center for Hierarchical Material Design (CHiMaD).

[1] S. Y. Chin, Y. C. Poh, A.-C. Kohler, J. T. Compton, L. L. Hsu, K. M. Lau, S. Kim, B. W. Lee., F. Y. Lee, and S. K. Sia, Additive manufacturing of hydrogel-based materials for next-generation implantable medical devices, Sci. Rob. **2**, eaah6451 (2017).

[2] I. Gibson, D. Rosen, and B. Stucker, *Additive Manufacturing Technologies: 3D Printing, Rapid Prototyping and Direct Digital Manufacturing* (Springer, New York, 2015).

[3] Y. He, G. Xue, and J. Fu, Fabrication of low cost soft tissue prostheses with the desktop 3D printer, Sci. Rep. **4**, 6973 (2014).

[4] D. C. Hofmann, S. Roberts, R. Otis, J. Kolodziejska, R. P. Dillon, J.-O. Suh, A. A. Shapiro, Z-K. Liu, and J.-P. Borgonia, Developing gradient metal alloys through radial deposition additive manufacturing, Sci. Rep. **4**, 5357 (2014).

[5] J. S. Miller, K. R. Stevens, M. T. Yang, B. M. Baker, D.-H. T. Nguyen, D. M. Cohen, E. Toro, A. A. Chen, P. A. Galie, X. Yu, R. Chaturvedi, S. N. Bhatia, and C. S. Chen, Rapid casting of patterned vascular networks for perfusable engineered three-dimensional tissues, Nat. Mater. **11**, 768 (2012).

[6] T. Mukherjee, J. S. Zuback, A. De, and T. DebRoy, Printability of alloys for additive manufacturing, Sci. Rep. **6**, 19717 (2016).

[7] S. V. Murphy and A. Atala, 3D bioprinting of tissues and organs, Nat. Biotechnol. **32**, 773 (2014).

[8] U. G. K. Wegst, H. Bai, E. Saiz, A. P. Tomsia, and R. O. Ritchie, Bioinspired structural materials, Nat. Mater. **14**, 23 (2015).

[9] W. K. C. Yung, B. Sun, Z. Meng, J. Huang, Y. Jin, H. S. Choy, Z. Cai, G. Li, C. L. Ho, J. Yang, and W. Y. Wong, Additive and photochemical manufacturing of copper, Sci. Rep. **6**, 39584 (2016).

[10] Y. Zheng, Z. He, Y. Gao, and J. Liu, Direct desktop printed-circuits-on-paper flexible electronics, Sci. Rep. **3**, 1786 (2013).
[11] W. J. Sames, F. A. List, S. Pannala, R. R. Dehoff, and S. S. Babu, The metallurgy and processing science of metal additive manufacturing, Int. Mater. Rev. **61**, 315 (2016).
[12] M. J. Matthews, G. Guss, S. A. Khairallah, A. M. Rubenchik, P. J. Depond, and W. E. King, Denudation of metal powder layers in laser powder bed fusion processes, Acta Mater. **114**, 33 (2016).
[13] S. H. Davis, Thermocapillary instabilities, Annu. Rev. Fluid Mech. **19**, 403 (1987).
[14] S. A. Khairallah, A. T. Anderson, A. Rubenchik, and W. E. King, Laser powder-bed fusion additive manufacturing: Physics of complex melt flow and formation mechanisms of pores, spatter, and denudation zones, Acta Mater. **108**, 36 (2016).
[15] K. N. Kowal, S. H. Davis, and P. W. Voorhees, Instabilities in rapid directional solidification under weak flow, Phys. Rev. E **96**, 062802 (2017).
[16] K. N. Kowal, S. H. Davis, and P. W. Voorhees, Thermocapillary instabilities in a horizontal liquid layer under partial basal slip, J. Fluid Mech. **855**, 839 (2018).
[17] K. N. Kowal, A. L. Altieri, and S. H. Davis, Strongly nonlinear theory of rapid solidification near absolute stability, Phys. Rev. E **96**, 042801 (2017).
[18] J. R. A. Pearson, On convection cells induced by surface tension, J. Fluid Mech. **4**, 489 (1958).
[19] M. Takashima, Surface tension driven instability in a horizontal liquid layer with a deformable free surface. I. Stationary convection, J. Phys. Soc. Jpn. **50**, 2745 (1981).
[20] P. J. Saenz, P. Valluri, K. Sefiane, G. Karapetsas, and O. K. Matar, Linear and nonlinear stability of hydrothermal waves in planar liquid layers driven by thermocapillarity, Phys. Fluids **25**, 094101 (2013).
[21] A. K. Sen and S. H. Davis, Steady thermocapillary flows in two-dimensional slots, J. Fluid Mech. **121**, 163 (1982).
[22] M. K. Smith and S. H. Davis, Instabilities of dynamic thermocapillary liquid layers. Part 1. Convective instabilities, J. Fluid Mech. **132**, 119 (1983).
[23] M. K. Smith and S. H. Davis, Instabilities of dynamic thermocapillary liquid layers. Part 2. Surface-wave instabilities, J. Fluid Mech. **132**, 145 (1983).
[24] M. K. Smith, The nonlinear stability of dynamic thermocapillary liquid layers, J. Fluid Mech. **194**, 391 (1988).
[25] A. Zebib, G. M. Homsy, and E. Meiburg, High Marangoni number convection in a square cavity, Phys. Fluids **28**, 3467 (1985).
[26] B. M. Carpenter and G. M. Homsy, High Marangoni number convection in a square cavity: Part II, Phys. Fluids A **2**, 137 (1990).
[27] J.-C. Chen and F.-S. Hwu, Oscillatory thermocapillary flow in a rectangular cavity, Int. J. Heat Mass Transfer **36**, 3743 (1993).
[28] M. Mundrane, J. Xu, and A. Zebib, Thermocapillary convection in a rectangular cavity with a deformable interface, Adv. Space Res. **16**, 41 (1995).
[29] J. Xu and A. Zebib, Oscillatory two- and three-dimensional thermocapillary convection, J. Fluid Mech. **364**, 187 (1998).
[30] M. Hamed and J. M. Floryan, Marangoni convection. Part 1. A cavity with differentially heated sidewalls, J. Fluid Mech. **405**, 79 (2000).
[31] S. J. Cowley and S. H. Davis, Viscous thermocapillary convection at high Marangoni number, J. Fluid Mech. **135**, 175 (1983).
[32] H. J. Palmer and J. C. Berg, Convective instability in liquid pools heated from below, J. Fluid Mech. **47**, 779 (1971).
[33] A. Juel, T. Mullin, H. Ben Hadid, and D. Henry, Three-dimensional free convection in molten gallium, J. Fluid Mech. **436**, 267 (2001).
[34] B. Hof, A. Juel, L. Zhao, D. Henry, H. Ben Hadid, and T. Mullin, On the onset of oscillatory convection in molten gallium, J. Fluid Mech. **515**, 391 (2004).
[35] W. J. Boettinger, D. Shechtman, R. J. Schaefer, and F. S. Biancaniello, The effect of rapid solidification velocity on the microstructure of Ag-Cu alloys, Metall. Trans. A **15**, 55 (1984).
[36] M. Gremaud, M. Carrard, and W. Kurz, The microstructure of rapidly solidified Al-Fe alloys subjected to laser surface treatment, Acta Metall. Mater. **38**, 2587 (1990).
[37] M. Gremaud, M. Carrard, and W. Kurz, Banding phenomena in Al-Fe alloys subjected to laser surface treatment, Acta Metall. Mater. **39**, 1431 (1991).
[38] W. Kurz and R. Trivedi, Acta Metall. Mater. **38**, 1 (1990).
[39] K. N. Kowal and S. H. Davis, Strong shear-flow modulation of instabilities in rapid directional solidification, Acta Mater. **164**, 464 (2019).